

## **CAM-CLAY PLASTICITY, PART I: IMPLICIT INTEGRATION OF ELASTO-PLASTIC CONSTITUTIVE RELATIONS**

**Ronaldo I. BORJA and Seung R. LEE**

*Department of Civil Engineering, Stanford University, Stanford, CA 94305, U.S.A.*

Received 8 July 1988

Revised manuscript received 8 February 1989

Two stress integration algorithms based on implicit calculation of plastic strain are implemented and tested for the modified Cam–Clay plasticity model. The integration rules fall under the category of return mapping algorithms in which the return directions are computed by closest point projection for associative flow rule and by central return mapping for non-associative flow rule applied to the Cam–Clay ellipsoids. Stress updates take place at the Gauss points upon enforcement of the consistency condition in which the appropriate consistency parameters are determined iteratively on the scalar level. Numerical examples with geotechnical applications, which include an analysis of foundation bearing capacity and an investigation of deformations in vertical cuts, are discussed to demonstrate the global accuracy and stability of the numerical solution. The relationships among various return mapping schemes are discussed in the context of both associative and non-associative flow rule formulations.

### **1. Introduction**

Cam–Clay models are thus far the most widely used plasticity models for characterizing the stress–strain behavior of cohesive soils subjected to three-dimensional state of stress [1–8]. The advantages of these models lie in their apparent simplicity and their capability to represent the stress–strain behavior of soils realistically. Cam–Clay models include features such as pressure sensitivity, hardening and softening responses typical in soils, and require (few) parameters which can be directly obtained from conventional laboratory tests [2, 3, 9].

In the context of finite element analysis, the solution of boundary value problems with Cam–Clay application requires the use of numerical integration procedures for describing the incremental evolution of stresses and hardening parameters. Usually, in the literature, however, little information is given on the details of how these models have been implemented in the program (see e.g. [4] for a comprehensive list of computer packages with critical state model applications). It appears that most integration algorithms dealing with the incremental solution of constitutive relations with Cam–Clay applications are still based on explicit integration of stresses [4, 10], albeit implicit return mapping algorithms have already been tested and applied to simple plasticity models such as the linearly hardening Von Mises and Drucker–Prager yield models [11–15]. Return mapping algorithms for the integration of elasto-plastic constitutive equations have been shown to exhibit good accuracy and stability properties when tested using these simple models [11, 12, 15].

Recent development on alternative formulations for the Cam-Clay and cap models indicates that, from computations of isoerror maps, implicit return mapping algorithms also lead to good solution accuracy when applied to more complicated models where less trivial return paths are involved [5, 14]. However, no global implementation, practical applications and performance evaluation of iterative procedures germane to this type of solution have been reported thus far in the literature [7].

In this paper, implicit formulations for the integration of rate constitutive relations applicable to a Cam-Clay model are discussed and implemented in the context of return mapping algorithms. The version of the model investigated in this paper is the modified Cam-Clay model described in [1, 2, 8]. Return mapping schemes based on closest point projection algorithm for associative flow rule [5, 13, 14] and central return mapping for a non-associative flow rule [7, 16] are implemented and tested. Both formulations show a remarkable solution accuracy and, upon consistent linearization of the incremental equations, result in an iterative solution scheme which is shown to exhibit quadratic rate of convergence in Newton's method in both the residual force and energy norms. The relationships among various return mapping algorithms are established in the context of both the associative and the non-associative flow rule formulations. Numerical examples with geotechnical applications are presented to assess the performance of the proposed algorithms.

## 2. Cam-Clay equations: associative flow rule

In this section we outline briefly the main features of the subject constitutive model. Details and additional descriptions may be found in [1, 2, 6, 8]. Following the notations used in [2, 6], we define the volumetric stress  $p$  and the deviatoric stress  $q$  as

$$p = \frac{1}{3} \text{tr}(\boldsymbol{\sigma}), \quad q = \sqrt{\frac{3}{2}} \|\boldsymbol{\xi}\|, \quad (2.1)$$

where  $\boldsymbol{\sigma}$  is the Cauchy stress tensor and  $\boldsymbol{\xi} = \boldsymbol{\sigma} - \frac{1}{3} \text{tr}(\boldsymbol{\sigma})\mathbf{1}$ , with  $\mathbf{1}_{ij} = \delta_{ij}$ , the Kronecker delta. The ellipsoid of the modified Cam-Clay model is of the form

$$F = \frac{q^2}{M^2} + p(p - p_c) = 0, \quad (2.2)$$

where  $M$  is the slope of the critical state line [6, 8] and  $p_c$ , called the preconsolidation pressure, is the diameter of the ellipsoid in the direction of the axis  $p$  (Fig. 1). The hardening function in rate form is given by

$$\dot{p}_c = \vartheta p_c \dot{\epsilon}_v^p, \quad \dot{\epsilon}_v^p = \text{tr}(\dot{\epsilon}^p), \quad \vartheta = \frac{1+e}{\lambda - \kappa}, \quad (2.3)$$

where  $\dot{\epsilon}^p$  is the plastic strain rate tensor,  $e$  is the void ratio of the soil mass,  $\lambda$  is the virgin compression index and  $\kappa$  is the swell/recompression index. Both  $\lambda$  and  $\kappa$  are assumed constant and are usually determined from one-dimensional consolidation tests. The soil's void ratio  $e$  is a state variable and, therefore, so is  $\vartheta$ . However the variation of  $e$  is usually small even for

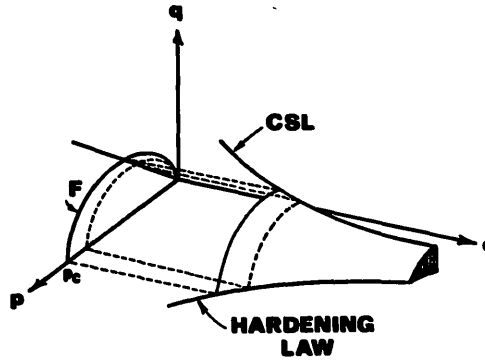


Fig. 1. Yield criterion and hardening law.

large load increments [3]. Consequently, both  $e$  and  $\vartheta$  will be treated explicitly in this paper and will be assumed constant over the time interval  $[t_n, t_{n+1}]$ , i.e.,  $\vartheta = \vartheta_n = (1 + e_n)/(\lambda - \kappa)$  within this time interval.

The use of the associative flow rule enables one to express  $\dot{\epsilon}^p$  as

$$\dot{\epsilon}^p = \dot{\phi} \frac{\partial F}{\partial \sigma}, \quad (2.4)$$

with  $\partial F / \partial \sigma$  obtained from a direct application of the chain rule as follows [2]:

$$\frac{\partial F}{\partial \sigma} = \frac{\partial F}{\partial p} \frac{\partial p}{\partial \sigma} + \frac{\partial F}{\partial q} \frac{\partial q}{\partial \sigma} = \frac{1}{3} \left( \frac{\partial F}{\partial p} \right) \mathbf{1} + \sqrt{\frac{3}{2}} \left( \frac{\partial F}{\partial q} \right) \hat{n}, \quad (2.5)$$

where  $\hat{n} = \xi / \|\xi\|$  and  $\dot{\phi}$  is a factor. The derivatives of  $F$  with respect to  $p$ ,  $q$  and  $p_c$  can be obtained from (2.2) as follows:

$$\frac{\partial F}{\partial p} = 2p - p_c, \quad \frac{\partial F}{\partial q} = \frac{2q}{M^2}, \quad \frac{\partial F}{\partial p_c} = -p. \quad (2.6)$$

Equations (2.3) and (2.4) may be integrated over a finite time increment either analytically or by employing the generalized trapezoidal method with respect to the variable  $p_c$ . Integrating (2.3) and (2.4) over a finite time increment yields the following alternative incremental hardening laws:

$$(p_c)_{n+1} = (p_c)_n \exp(\vartheta \Delta \epsilon_v^p) \quad (2.7a)$$

from analytical integration and

$$(p_c)_{n+1} = \frac{1 + \vartheta(1 - \alpha)\Delta \epsilon_v^p}{1 - \vartheta\alpha\Delta \epsilon_v^p} (p_c)_n \quad (2.7b)$$

from trapezoidal integration, where  $0 \leq \alpha \leq 1$  is the trapezoidal integration parameter,  $(p_c)_n$  is the converged preconsolidation pressure of the previous time step, and

$$\Delta \epsilon_v^p = \Delta \phi \operatorname{tr} \left( \frac{\partial F}{\partial \sigma} \right) = \Delta \phi \frac{\partial F}{\partial p}. \quad (2.8)$$

In (2.7b)  $\alpha = 0$  corresponds to explicit integration, while  $\alpha = 1.0$  corresponds to implicit integration.

The conventional solution of incremental plasticity problems is based on explicit integration of the following rate constitutive equation (see [10]):

$$\dot{\sigma} = c^{ep} : \dot{\epsilon}; \quad c^{ep} = c^e - \langle c^p \rangle, \quad (2.9)$$

in which  $c^e$  is the elastic stress-strain tensor given by

$$c^e = K \mathbf{1} \otimes \mathbf{1} + 2\mu (\mathbf{I} - \frac{1}{3} \mathbf{1} \otimes \mathbf{1}), \quad (2.10)$$

$c^p$  is the plastic stress-strain tensor, and the symbols ' $\langle \cdot \rangle$ ' are the Macauley brackets which imply that  $\langle \cdot \rangle = \cdot$  if plasticity is in effect, and  $\langle \cdot \rangle = 0$  otherwise. With the expanding ellipsoids given by (2.2),  $c^p$  is obtained as [2]

$$\begin{aligned} c^p &= \chi^{-1} \left( c^e : \frac{\partial F}{\partial \sigma} \otimes \frac{\partial F}{\partial \sigma} : c^e \right) \\ &= \chi^{-1} \left[ \left( K \frac{\partial F}{\partial p} \right)^2 \mathbf{1} \otimes \mathbf{1} + \sqrt{\frac{3}{2}} \left( K \frac{\partial F}{\partial p} \right) \left( 2\mu \frac{\partial F}{\partial q} \right) (\hat{n} \otimes \mathbf{1} + \mathbf{1} \otimes \hat{n}) \right. \\ &\quad \left. + \frac{3}{2} \left( 2\mu \frac{\partial F}{\partial q} \right)^2 \hat{n} \otimes \hat{n} \right], \end{aligned} \quad (2.11)$$

where

$$\begin{aligned} \chi &= \frac{\partial F}{\partial \sigma} : c^e : \frac{\partial F}{\partial \sigma} - \vartheta p_c \frac{\partial F}{\partial p} \frac{\partial F}{\partial p_c} \\ &= K \left( \frac{\partial F}{\partial p} \right)^2 + 3\mu \left( \frac{\partial F}{\partial q} \right)^2 + \vartheta p p_c \frac{\partial F}{\partial p}. \end{aligned} \quad (2.12)$$

In (2.10)–(2.12),  $\mathbf{I}$  is the identity tensor defined such that  $I_{ijkl} = \frac{1}{2}(\delta_{ik}\delta_{jl} + \delta_{il}\delta_{jk})$ , the symbol ' $\otimes$ ' denotes a tensor product in the sense that  $(a \otimes b)_{ijkl} = (a)_{ij}(b)_{kl}$  for any second order tensors  $a$  and  $b$ ,  $K$  is the elastic bulk modulus and  $\mu$  is the elastic shear modulus.

A feature which makes the Cam-Clay model different from conventional plasticity models is that the elastic moduli  $K$  and  $\mu$  in this model are likewise state variables. For example, in the extended three-dimensional models presented in [1, 17],

$$K = \frac{1+e}{\kappa} p \quad \text{and} \quad \mu = \frac{3K(1-2\nu)}{2(1+\nu)}, \quad (2.13)$$

where  $\nu$  is the elastic Poisson's ratio. The coupling of elastic shear and bulk moduli indicated in (2.13) may lead to a non-conservative model in which energy may be extracted from certain

loading cycles [17]. However, this fact may not be too important in practice if monotonic loading is considered [4], and hence (2.13) is still widely used. Equation (2.13) shows a model exhibiting a nonlinear elastic response which, when solved in conjunction with Cam–Clay plasticity by a fully implicit Newton’s method, may prove exceedingly laborious and computationally unattractive [5]. For these reasons,  $K$  and  $\mu$  in this paper will also be treated explicitly such that, over  $[t_n, t_{n+1}]$ ,  $K = K_n = (1 + e_n)p_n/\kappa$  and  $\mu = \mu_n = \frac{3}{2}K_n(1 - 2\nu)/(1 + \nu)$ .

### 3. Associative flow rule: closest point projection

#### 3.1. Preliminaries

In this section we present some of the identities used in subsequent derivations. Complete proofs and details can be found in [13].

Let  $\Delta \epsilon_{n+1}^k = \epsilon_{n+1}^k - \epsilon_n$ ,  $\sigma_{n+1}^{\text{tr}} = \sigma_n + c^e : \Delta \epsilon_{n+1}^k$ ,  $\xi_{n+1}^{\text{tr}} = \sigma_{n+1}^{\text{tr}} - \frac{1}{3} \text{tr}(\sigma_{n+1}^{\text{tr}}) \mathbf{1}$ , and consider the trial stress invariants

$$p_{n+1}^{\text{tr}} = \frac{1}{3} \text{tr}(\sigma_{n+1}^{\text{tr}}), \quad q_{n+1}^{\text{tr}} = \sqrt{\frac{3}{2}} \|\xi_{n+1}^{\text{tr}}\|, \quad (3.1)$$

where  $\sigma_n$  and  $\epsilon_n$  are the converged stress and strain tensors of the previous time step, respectively, the subscript  $n$  refers to time step number and the superscript  $k$  refers to an iteration counter. The derivatives of  $p_{n+1}^{\text{tr}}$  and  $q_{n+1}^{\text{tr}}$  with respect to  $\epsilon_{n+1}^k$  are

$$\frac{\partial p_{n+1}^{\text{tr}}}{\partial \epsilon_{n+1}^k} = K \mathbf{1}, \quad \frac{\partial q_{n+1}^{\text{tr}}}{\partial \epsilon_{n+1}^k} = 2\mu \sqrt{\frac{3}{2}} \hat{n}, \quad (3.2)$$

where  $\hat{n} = \xi_{n+1}^{\text{tr}} / \|\xi_{n+1}^{\text{tr}}\|$  is a unit tensor in the radial direction  $\xi_{n+1}^{\text{tr}}$ . In subsequent developments, the variation of the tensor  $\hat{n}$  with respect to  $\epsilon_{n+1}^k$  will be required and we present this derivative herein, from a straightforward application of the chain rule, without proof (see [13]):

$$\frac{\partial \hat{n}}{\partial \epsilon_{n+1}^k} = \frac{\partial \hat{n}}{\partial \xi_{n+1}^{\text{tr}}} : \frac{\partial \xi_{n+1}^{\text{tr}}}{\partial \epsilon_{n+1}^k} = 2\mu \frac{\partial \hat{n}}{\partial \xi_{n+1}^{\text{tr}}} : \frac{\partial \Delta \gamma_{n+1}^k}{\partial \epsilon_{n+1}^k} = \frac{2\mu}{\|\xi_{n+1}^{\text{tr}}\|} (\mathbf{I} - \frac{1}{3} \mathbf{1} \otimes \mathbf{1} - \hat{n} \otimes \hat{n}), \quad (3.3)$$

where  $\Delta \gamma_{n+1}^k = \Delta \epsilon_{n+1}^k - \frac{1}{3} \text{tr}(\Delta \epsilon_{n+1}^k) \mathbf{1}$ .

#### 3.2. Stress integration algorithm

We begin by writing the return mapping tensor equations depicted in Fig. 2 in the following form:

$$\sigma_{n+1}^k = \sigma_{n+1}^{\text{tr}} - c^e : \Delta \epsilon^p. \quad (3.4)$$

Consider the following volumetric part of  $\sigma_{n+1}^k$ :

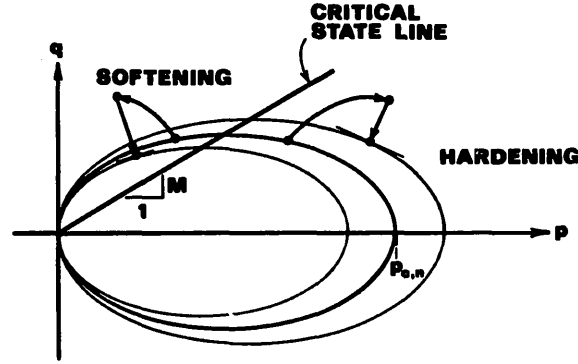


Fig. 2. Associative flow rule degenerates to a geometric closest point projection on  $F$  when  $K=3\mu$ .

$$p \equiv p_{n+1}^k = \frac{1}{3} \text{tr}(\sigma_{n+1}^k) = p_{n+1}^{\text{tr}} - K\Delta\epsilon_v^p, \quad (3.5)$$

where  $p_{n+1}^{\text{tr}} = \frac{1}{3} \text{tr}(\sigma_{n+1}^{\text{tr}})$  and  $\Delta\epsilon_v^p = \text{tr}(\Delta\epsilon^p)$ . Also, consider its deviatoric part

$$q \equiv q_{n+1}^k = \sqrt{\frac{3}{2}} \|\xi_{n+1}^k\| = \sqrt{\frac{3}{2}} \|\xi_{n+1}^{\text{tr}} - 2\mu\Delta\gamma^p\|, \quad (3.6)$$

where  $\xi_{n+1}^k = \sigma_{n+1}^k - p\mathbf{1}$ ,  $\xi_{n+1}^{\text{tr}} = \sigma_{n+1}^{\text{tr}} - p_{n+1}^{\text{tr}}\mathbf{1}$  and  $\Delta\gamma^p = \Delta\epsilon^p - \frac{1}{3}\Delta\epsilon_v^p\mathbf{1}$ . Invoking these definitions in (3.4) yields the following return mapping equations on the  $\pi$ -plane:

$$\xi_{n+1}^k = \xi_{n+1}^{\text{tr}} - 2\mu\Delta\gamma^p. \quad (3.7)$$

Since from flow rule equations (2.4) and (2.5),  $\Delta\gamma^p = \Delta\phi\sqrt{\frac{3}{2}}(\partial F/\partial q)\xi_{n+1}^{\text{tr}}/\|\xi_{n+1}^{\text{tr}}\|$ , it follows that  $\xi_{n+1}^{\text{tr}}$ ,  $\xi_{n+1}^k$  and  $\Delta\gamma^p$  have the same directions, i.e.,

$$\hat{n} = \frac{\xi_{n+1}^{\text{tr}}}{\|\xi_{n+1}^{\text{tr}}\|} = \frac{\xi_{n+1}^k}{\|\xi_{n+1}^k\|} = \frac{\Delta\gamma^p}{\|\Delta\gamma^p\|}, \quad (3.8)$$

so that

$$q = \sqrt{\frac{3}{2}} \|\xi_{n+1}^{\text{tr}}\| - 2\mu\sqrt{\frac{3}{2}} \|\Delta\gamma^p\| = q_{n+1}^{\text{tr}} - 3\mu\Delta\gamma^p, \quad (3.9)$$

where  $q_{n+1}^{\text{tr}} = \sqrt{\frac{3}{2}} \|\xi_{n+1}^{\text{tr}}\|$  and  $\Delta\gamma^p = \sqrt{\frac{2}{3}} \|\Delta\gamma^p\|$ .

Applying the normality rule over a finite time increment on  $\Delta\epsilon^p$  results in the following scalar equations:

$$p = p(\Delta\phi) = p_{n+1}^{\text{tr}} - K\Delta\phi \frac{\partial F}{\partial p} = p_{n+1}^{\text{tr}} - K\Delta\phi(2p - p_c), \quad (3.10a)$$

$$q = q(\Delta\phi) = q_{n+1}^{\text{tr}} - 3\mu\Delta\phi \frac{\partial F}{\partial q} = q_{n+1}^{\text{tr}} / \left(1 + 6\mu \frac{\Delta\phi}{M^2}\right), \quad (3.10b)$$

where  $\Delta\phi = \Delta\phi(\epsilon_{n+1}^k)$  is a scalar consistency parameter. The incremental hardening law may again be expressed either from the analytical solution

$$p_c = p_c(\Delta\phi) = (p_c)_n \exp \left( \vartheta \Delta\phi \frac{\partial F}{\partial p} \right) = (p_c)_n \exp [\vartheta \Delta\phi (2p - p_c)], \quad (3.10c)$$

or from the approximate trapezoidal integration

$$p_c = p_c(\Delta\phi) = \frac{1 + \vartheta(1 - \alpha)\Delta\phi(2p - p_c)}{1 - \vartheta\alpha\Delta\phi(2p - p_c)} (p_c)_n. \quad (3.10d)$$

**REMARK 3.1.** The use of a scalar stress mapping via the invariants  $p$  and  $q$ , rather than via the stress tensor  $\sigma$  itself, enables one to determine the consistency parameter  $\Delta\phi$  iteratively on the scalar level.

**REMARK 3.2.** Note from (3.10a) and (3.10b) that when  $K = 3\mu$ , the above mapping scheme degenerates to a geometric closest point projection on the ellipses drawn on the  $p$ - $q$  plane (Fig. 2).

**REMARK 3.3.** Choosing the exponential hardening law (3.10c) will eventually lead to two nested local Newton iteration loops (or three nested loops overall, including the global solution) as explained in Section 3.3. Choosing the (approximate) incremental hardening law (3.10d) will eliminate the innermost iteration loop, but at the expense of accuracy. As will be shown from solved examples, however, the additional expense engendered by a third (innermost) Newton iteration loop with use of (3.10c) is minimal particularly for a large mesh size. Thus, the exponential incremental hardening law (3.10c) describing the evolution of  $p_c$  will be considered in this paper.

### 3.3. Determination of the scalar consistency parameter

The parameter  $\Delta\phi$  in (3.10a)–(3.10c) is computed by imposing the consistency requirement

$$F = F(\Delta\phi) = \frac{q^2}{M^2} + p(p - p_c) = 0. \quad (3.11)$$

In determining the zero of this function, one can perform a local Newton iteration on the simultaneous nonlinear equation (3.10a)–(3.10c) and (3.11) to obtain the roots  $p_{n+1}^k$ ,  $q_{n+1}^k$ ,  $(p_c)_{n+1}^k$  and  $\Delta\phi^k$ , with initial estimates taken as  $\Delta\phi = 0$ ,  $p = p_{n+1}^{ir}$ ,  $q = q_{n+1}^{ir}$  and  $p_c = (p_c)_n$ . Alternatively, one can view (3.11) as a scalar nonlinear function whose root  $\Delta\phi^k$  gives the zero of  $F$ . This root can be solved using a local Newton iteration applied to the scalar function  $F$  as shown in Table 1.

Table 1  
Local Newton algorithm for computing the zero of  $F$

- 
1. Initialize  $k = 0$ ,  $\Delta\phi^k = 0$
  2. Compute  $F^k = F(\Delta\phi^k)$ , see Table 2
  3. If  $|F^k| < \text{FTOL}$ , exit; else
  4.  $\Delta\phi^{k+1} = \Delta\phi^k - F^k / F'(\Delta\phi^k)$
  5.  $k \leftarrow k + 1$  and go to 2.
-

In computing the derivative of  $F$  for use in Table 1, one can employ the chain rule on  $F$  as follows:

$$F'(\Delta\phi) = \frac{\partial F}{\partial p} \frac{\partial p}{\partial \Delta\phi} + \frac{\partial F}{\partial q} \frac{\partial q}{\partial \Delta\phi} + \frac{\partial F}{\partial p_c} \frac{\partial p_c}{\partial \Delta\phi}, \quad (3.12)$$

where  $\partial F/\partial p$ ,  $\partial F/\partial q$  and  $\partial F/\partial p_c$  are given by (2.6). Differentiating (3.10a)–(3.10c) implicitly results in

$$\frac{\partial p}{\partial \Delta\phi} = -K \frac{(2p - p_c)}{1 + (2K + \vartheta p_c)\Delta\phi}, \quad (3.13a)$$

$$\frac{\partial q}{\partial \Delta\phi} = -\frac{q}{\Delta\phi + M^2/6\mu}, \quad (3.13b)$$

$$\frac{\partial p_c}{\partial \Delta\phi} = \vartheta p_c \frac{(2p - p_c)}{1 + (2K + \vartheta p_c)\Delta\phi}. \quad (3.13c)$$

Since the variables  $p$  and  $p_c$  are coupled via (3.10a) and the nonlinear equation (3.10c), one cannot evaluate the function  $F(\Delta\phi^k)$  explicitly. Consequently,  $p$  and  $p_c$  will have to be solved iteratively. Rewriting (3.10a) in the form

$$p = \frac{p_{n+1}^{\text{tr}} + \Delta\phi^k K p_c}{1 + 2\Delta\phi^k K} \quad (3.14)$$

and substituting in (3.10c) gives

$$G = G(p_c) = (p_c)_n \exp\left(\vartheta \Delta\phi^k \frac{2p_{n+1}^{\text{tr}} - p_c}{1 + 2\Delta\phi^k K}\right) - p_c = 0. \quad (3.15)$$

We can then determine the root  $p_c = (p_c)_{n+1}^k$  of (3.15) which gives the zero of  $G$  iteratively by using a sub-local Newton scheme shown in the flow chart of Table 2.

**REMARK 3.4.** The above algorithm for determining the consistency parameter  $\Delta\phi$  is implementationally more adaptable to the Cam–Clay model than is the closest point projection algorithm for cap mode presented in [14] (cf. Box 4 of [14]), in which the consistency parameter is taken as  $\frac{1}{2} p_c (= \kappa_{n+1}^k$  in their notation) instead of  $\Delta\phi$ . The latter algorithm ceases

Table 2  
Sub-local Newton algorithm for computing the zero of  $G$

1. Initialize  $j = 0$ ,  $p_c^j = (p_c)_n$
2. Compute  $G^j = G(p_c^j)$
3. If  $|G^j| < \text{GTOL}$ , go to 6; else
4.  $p_c^{j+1} = p_c^j - G^j/G'(p_c^j)$
5.  $j \leftarrow j + 1$  and go to 2
6. Solve  $F^k = F(\Delta\phi^k, p^k, q^k, p_c^k)$  and return.



to become applicable when  $p_{n+1}^{\text{tr}} > (p_c)_n$  in which case, the function ' $F_c$ ' in Box 4 of [14] (which is equivalent to the variable  $q$  in this paper) cannot be evaluated.

### 3.4. Determination of the consistent tangential moduli

Let the incremental response function corresponding to the strain tensor increment  $\epsilon_{n+1}^k - \epsilon_n$  be written in the following form:

$$\sigma_{n+1}^k = \frac{1}{3} \text{tr}(\sigma_{n+1}^k) \mathbf{1} + \|\xi_{n+1}^k\| \hat{n} = p \mathbf{1} + \sqrt{\frac{2}{3}} q \hat{n}. \quad (3.16)$$

The consistent tangential moduli can then be obtained by directly evaluating the variation

$$c_{n+1}^k = \frac{\partial \sigma_{n+1}^k}{\partial \epsilon_{n+1}^k} = \mathbf{1} \otimes \frac{\partial p}{\partial \epsilon_{n+1}^k} + \sqrt{\frac{2}{3}} q \frac{\partial \hat{n}}{\partial \epsilon_{n+1}^k} + \sqrt{\frac{2}{3}} \hat{n} \otimes \frac{\partial q}{\partial \epsilon_{n+1}^k}. \quad (3.17)$$

Evaluating the derivatives in (3.17) implicitly from (3.10a)–(3.10c) yields

$$\begin{aligned} \frac{\partial p}{\partial \epsilon_{n+1}^k} &= \frac{\partial p_{n+1}^{\text{tr}}}{\partial \epsilon_{n+1}^k} - K \left[ \Delta \phi \left( 2 \frac{\partial p}{\partial \epsilon_{n+1}^k} - \frac{\partial p_c}{\partial \epsilon_{n+1}^k} \right) + (2p - p_c) \frac{\partial \Delta \phi}{\partial \epsilon_{n+1}^k} \right] \\ &= a_1 K \mathbf{1} + a_2 K \frac{\partial \Delta \phi}{\partial \epsilon_{n+1}^k}, \end{aligned} \quad (3.18)$$

where

$$a_1 = (1 + p_c \vartheta \Delta \phi) / a, \quad a_2 = -(2p - p_c) / a \quad \text{and} \quad a = 1 + 2K \Delta \phi + p_c \vartheta \Delta \phi. \quad (3.19)$$

The derivative of  $p_c$  with respect to  $\epsilon_{n+1}^k$  is

$$\begin{aligned} \frac{\partial p_c}{\partial \epsilon_{n+1}^k} &= p_c \vartheta \left[ \Delta \phi \left( 2 \frac{\partial p}{\partial \epsilon_{n+1}^k} - \frac{\partial p_c}{\partial \epsilon_{n+1}^k} \right) + (2p - p_c) \frac{\partial \Delta \phi}{\partial \epsilon_{n+1}^k} \right] \\ &= a_3 K \mathbf{1} + a_4 K \frac{\partial \Delta \phi}{\partial \epsilon_{n+1}^k}, \end{aligned} \quad (3.20)$$

where

$$a_3 = 2p_c \vartheta \Delta \phi / a \quad \text{and} \quad a_4 = \vartheta \frac{p_c}{K} (2p - p_c) / a. \quad (3.21)$$

The second steps in (3.18) and (3.20) can be verified by solving simultaneously for  $\partial p / \partial \epsilon_{n+1}^k$  and  $\partial p_c / \partial \epsilon_{n+1}^k$ .

Finally, the derivative of  $q$  with respect to  $\epsilon_{n+1}^k$  is

$$\begin{aligned} \frac{\partial q}{\partial \epsilon_{n+1}^k} &= \frac{\partial q_{n+1}^{\text{tr}}}{\partial \epsilon_{n+1}^k} - \frac{6\mu \Delta \phi}{M^2} \frac{\partial q}{\partial \epsilon_{n+1}^k} - \frac{6\mu q}{M^2} \frac{\partial \Delta \phi}{\partial \epsilon_{n+1}^k} \\ &= 2\mu a_5 \hat{n} + 2\mu a_6 \frac{\partial \Delta \phi}{\partial \epsilon_{n+1}^k}, \end{aligned} \quad (3.22)$$

where

$$a_5 = \sqrt{\frac{3}{2}} \left( 1 + 6\mu \frac{\Delta\phi}{M^2} \right)^{-1} \quad \text{and} \quad a_6 = -\frac{3q}{M^2} \left( 1 + 6\mu \frac{\Delta\phi}{M^2} \right)^{-1}. \quad (3.23)$$

The derivative  $\partial\Delta\phi/\partial\epsilon_{n+1}^k$  can be determined by imposing the scalar consistency requirement (3.11). Differentiating  $F = F(\Delta\phi(\epsilon_{n+1}^k))$  with respect to  $\epsilon_{n+1}^k$  results in

$$\frac{\partial F}{\partial \epsilon_{n+1}^k} = \frac{2q}{M^2} \frac{\partial q}{\partial \epsilon_{n+1}^k} + (2p - p_c) \frac{\partial p}{\partial \epsilon_{n+1}^k} - p \frac{\partial p_c}{\partial \epsilon_{n+1}^k} \equiv 0. \quad (3.24)$$

Substituting (3.18), (3.20) and (3.22) in (3.24) gives

$$\frac{\partial\Delta\phi}{\partial\epsilon_{n+1}^k} = b_1 \mathbf{1} + b_2 \hat{n}, \quad (3.25)$$

where

$$\begin{aligned} b_1 &= -K[(a_3 - 2a_1)p + a_1 p_c]/b, \\ b_2 &= 2\mu \frac{2q}{M^2} a_5/b, \\ b &= -2\mu \frac{2q}{M^2} a_6 - K[(2a_2 - a_4)p - a_2 p_c]. \end{aligned} \quad (3.26)$$

Substituting (3.25) in (3.18), (3.20) and (3.22) results in

$$\begin{aligned} \frac{\partial p}{\partial \epsilon_{n+1}^k} &= K(a_1 + a_2 b_1) \mathbf{1} + K(a_2 b_2) \hat{n}, \\ \frac{\partial q}{\partial \epsilon_{n+1}^k} &= 2\mu(a_6 b_1) \mathbf{1} + 2\mu(a_5 + a_6 b_2) \hat{n}, \\ \frac{\partial p_c}{\partial \epsilon_{n+1}^k} &= K(a_3 + a_4 b_1) \mathbf{1} + K(a_4 b_2) \hat{n}. \end{aligned} \quad (3.27)$$

Finally, substituting (3.27) and (3.3) in (3.17) produces the desired consistent tangential moduli

$$\begin{aligned} c_{n+1}^k &= 2\mu\xi \mathbf{I} + [K(a_1 + a_2 b_1) - \frac{1}{3}(2\mu)\xi] \mathbf{1} \otimes \mathbf{1} + K(a_2 b_2) \mathbf{1} \otimes \hat{n} \\ &\quad + 2\mu\sqrt{\frac{2}{3}}(a_6 b_1) \hat{n} \otimes \mathbf{1} + 2\mu[\sqrt{\frac{2}{3}}(a_5 + a_6 b_2) - \xi] \hat{n} \otimes \hat{n}, \end{aligned} \quad (3.28)$$

where  $\xi = \sqrt{\frac{2}{3}} q / \|\xi_{n+1}^k\| = \|\xi_{n+1}^k\| / \|\xi_{n+1}^k\|$ . Equation (3.28) is consistent with the linearization of  $\sigma_{n+1}^k$  and preserves the asymptotic rate of quadratic global convergence of Newton's method.

**REMARK 3.5.** It can be seen that (3.28) generally yields a nonsymmetric tangent operator albeit the flow rule is associative. This is true since in general,  $K(a_2 b_2) \neq 2\mu\sqrt{\frac{2}{3}}(a_6 b_1)$  due to the form of the incremental hardening law (2.7).

**REMARK 3.6.** It is noteworthy that when  $\Delta\phi \rightarrow 0$  (i.e., explicit),  $p_{n+1}^{\text{tr}} \rightarrow p$ ,  $q_{n+1}^{\text{tr}} \rightarrow q$  and  $\xi \rightarrow 1.0$ . Also, for this condition,  $a \rightarrow a_1 \rightarrow 1.0$ ,  $a_2 \rightarrow -\partial F/\partial p$ ,  $a_3 \rightarrow 0$ ,  $a_4 \rightarrow \vartheta(p_c/K)\partial F/\partial p$ ,  $a_5 \rightarrow \sqrt{3}/2$ ,  $a_6 \rightarrow -\frac{3}{2}\partial F/\partial q$ ; hence,  $b \rightarrow \chi$  (cf. (2.12)),  $b_1 \rightarrow -K(\partial F/\partial p)/\chi$ ,  $b_2 \rightarrow -(2\mu)\sqrt{3}/2(\partial F/\partial q)/\chi$ , and, therefore,  $c_{n+1}^k \rightarrow c^{\text{cp}}$ , i.e., the consistent tangent given by (3.28) degenerates to the (symmetric) continuum tangent given by (2.9)–(2.11).

#### 4. Nonassociative flow rule: central return mapping algorithm

Non-associative flow rules in conjunction with Cam–Clay plasticity models are often employed to better replicate the behavior of some soils for which the associative flow rule is less appropriate [4, 7, 16]. Consequently, return directions are often modified to reflect the non-associative yielding of the soil. In this section we consider a stress projection algorithm depicted in Fig. 3, in which stresses are mapped onto  $F$  in the direction of the center of the expanding ellipsoid (see [7] where this idea was proposed). This algorithm will generally lead to a non-associative flow rule based on a plastic potential  $Q$ , other than  $F$ , or may be interpreted as a numerical counterpart of a bounding surface plasticity model presented in [16] in which the return direction is consistent with the position of a vanishing elastic region on the  $p$ -axis inside the consolidation surface  $F$ . Note that this return mapping algorithm generally results in a non-associativeness only in bulk but not in the deviatoric plane where the flow rule remains associative.

##### 4.1. Stress integration algorithm

Consider the two similar triangles shown in Fig. 3. Integrating stresses implicitly by way of their invariants results in the following scalar equations:

$$p = p(\Delta\epsilon_v^p) = p_{n+1}^{\text{tr}} - K\Delta\epsilon_v^p, \quad (4.1a)$$

$$q = q(\Delta\epsilon_v^p) = q_{n+1}^{\text{tr}} \frac{p - \frac{1}{2}p_c}{p_{n+1}^{\text{tr}} - \frac{1}{2}p_c}, \quad (4.1b)$$

$$p_c = p_c(\Delta\epsilon_v^p) = (p_c)_n \exp(\vartheta\Delta\epsilon_v^p), \quad (4.1c)$$

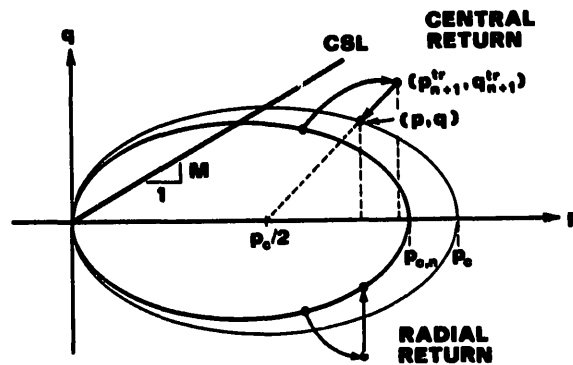


Fig. 3. Nonassociative flow rule: central and radial return mapping algorithms.

where  $p = p_{n+1}^k$ ,  $q = q_{n+1}^k$ ,  $p_c = (p_c)_{n+1}^k$  and  $\Delta \varepsilon_v^p = \Delta \varepsilon_v^p(\varepsilon_{n+1}^k)$ . In the above stress integration equations, the scalar consistency parameter is  $\Delta \varepsilon_v^p$ . It can be shown that the above return mapping scheme corresponds to the use of the (ellipsoidal) plastic potential.

$$Q = \theta a^2 + p(p - p_c) = 0, \quad (4.2)$$

where  $\theta = K/(3\mu)$ .

#### 4.2. Determination of the scalar consistency parameter

Imposing the consistency requirement on the yield function  $F$  gives

$$F = F(\Delta \varepsilon_v^p) = \frac{q^2}{M^2} + p(p - p_c) = 0, \quad (4.3)$$

where  $F$  is now a nonlinear function of  $\Delta \varepsilon_v^p$ . The value of  $\Delta \varepsilon_v^p$  which gives the zero of  $F$  can again be obtained by performing a local Newton iteration as summarized in Table 3.

The derivative of  $F(\Delta \varepsilon_v^p)$  for use in Table 3 can be obtained from (4.3) by employing the chain rule as follows:

$$F'(\Delta \varepsilon_v^p) = \frac{\partial F}{\partial p} \frac{\partial p}{\partial \Delta \varepsilon_v^p} + \frac{\partial F}{\partial q} \frac{\partial q}{\partial \Delta \varepsilon_v^p} + \frac{\partial F}{\partial p_c} \frac{\partial p_c}{\partial \Delta \varepsilon_v^p}, \quad (4.4)$$

where  $\partial F/\partial p$ ,  $\partial F/\partial q$  and  $\partial F/\partial p_c$  are summarized in (2.6) and

$$\begin{aligned} \frac{\partial p}{\partial \Delta \varepsilon_v^p} &= -K, \\ \frac{\partial q}{\partial \Delta \varepsilon_v^p} &= -\frac{q_{n+1}^{ir}}{p_{n+1}^{ir} - \frac{1}{2}p_c} \left[ K - \frac{1}{2}p_c \vartheta \frac{p_{n+1}^{ir} - p}{p_{n+1}^{ir} - \frac{1}{2}p_c} \right], \\ \frac{\partial p_c}{\partial \Delta \varepsilon_v^p} &= \vartheta p_c. \end{aligned} \quad (4.5)$$

Observe that since  $p$  and  $p_c$  in (4.1a, c) are uncoupled, an explicit evaluation of  $F$  in (4.3) is possible. Thus, this nonlinear solution scheme entails only two nested Newton iteration loops of implementation: a global iteration loop and a local (inner) iteration loop.

Table 3

Local Newton algorithm for computing the zero of  $F$

- 
1. Initialize  $k = 0$ ,  $(\Delta \varepsilon_v^p)^k = 0$
  2. Compute  $F^k = F((\Delta \varepsilon_v^p)^k)$
  3. If  $|F^k| < \text{FTOL}$ , exit; else
  4.  $(\Delta \varepsilon_v^p)^{k+1} = (\Delta \varepsilon_v^p)^k - F^k/F'((\Delta \varepsilon_v^p)^k)$
  5.  $k \leftarrow k + 1$  and go to 2.
-

### 4.3. Determination of the consistent tangential moduli

Following the procedure employed in the development of the consistent tangential tensor  $c_{n+1}^k$  of the preceding section, the incremental response function corresponding to the strain tensor increment  $\epsilon_{n+1}^k - \epsilon_n$  is again written as

$$\sigma_{n+1}^k = \frac{1}{3} \text{tr}(\sigma_{n+1}^k) \mathbf{1} + \|\xi_{n+1}^k\| \hat{n} = p \mathbf{1} + \sqrt{\frac{2}{3}} q \hat{n}, \quad (4.6)$$

where  $p = p_{n+1}^k = p(\epsilon_{n+1}^k)$ ,  $q = q_{n+1}^k = q(\epsilon_{n+1}^k)$  and  $\hat{n} = \xi_{n+1}^{\text{tr}} / \|\xi_{n+1}^{\text{tr}}\|$ . The tangential moduli consistent with this return mapping scheme is then obtained by directly evaluating the variation

$$c_{n+1}^k = \frac{\partial \sigma_{n+1}^k}{\partial \epsilon_{n+1}^k} = \mathbf{1} \otimes \frac{\partial p}{\partial \epsilon_{n+1}^k} + \sqrt{\frac{2}{3}} q \frac{\partial \hat{n}}{\partial \epsilon_{n+1}^k} + \sqrt{\frac{2}{3}} \hat{n} \otimes \frac{\partial q}{\partial \epsilon_{n+1}^k}. \quad (4.7)$$

From (4.1) the derivative of  $p$  with respect to  $\epsilon_{n+1}^k$  is

$$\frac{\partial p}{\partial \epsilon_{n+1}^k} = \frac{\partial p_{n+1}^{\text{tr}}}{\partial \epsilon_{n+1}^k} - K \frac{\partial \Delta \epsilon_v^p}{\partial \epsilon_{n+1}^k} = K \mathbf{1} - K \frac{\partial \Delta \epsilon_v^p}{\partial \epsilon_{n+1}^k}. \quad (4.8)$$

The derivative of  $p_c$  with respect to  $\epsilon_{n+1}^k$  is

$$\frac{\partial p_c}{\partial \epsilon_{n+1}^k} = p_c \vartheta \frac{\partial \Delta \epsilon_v^p}{\partial \epsilon_{n+1}^k}. \quad (4.9)$$

Finally, the derivative of  $q$  with respect to  $\epsilon_{n+1}^k$  is

$$\frac{\partial q}{\partial \epsilon_{n+1}^k} = K \alpha_1 \mathbf{1} + (2\mu) \alpha_2 \hat{n} + K \alpha_3 \frac{\partial \Delta \epsilon_v^p}{\partial \epsilon_{n+1}^k}, \quad (4.10)$$

where

$$\begin{aligned} \alpha_1 &= q_{n+1}^{\text{tr}} \frac{p_{n+1}^{\text{tr}} - p}{(p_{n+1}^{\text{tr}} - \frac{1}{2} p_c)^2}, \\ \alpha_2 &= \sqrt{\frac{3}{2}} \frac{p - \frac{1}{2} p_c}{p_{n+1}^{\text{tr}} - \frac{1}{2} p_c}, \\ \alpha_3 &= -\frac{q_{n+1}^{\text{tr}}}{p_{n+1}^{\text{tr}} - \frac{1}{2} p_c} \left( 1 + \vartheta \frac{p_c}{2K} \frac{p_{n+1}^{\text{tr}} - p}{p_{n+1}^{\text{tr}} - \frac{1}{2} p_c} \right). \end{aligned} \quad (4.11)$$

The derivative  $\partial \Delta \epsilon_v^p / \partial \epsilon_{n+1}^k$  is obtained from the scalar consistency equation (4.3). Differentiating  $F$  with respect to  $\epsilon_{n+1}^k$  results in

$$\frac{\partial F}{\partial \epsilon_{n+1}^k} = \frac{2q}{M^2} \frac{\partial q}{\partial \epsilon_{n+1}^k} + (2p - p_c) \frac{\partial p}{\partial \epsilon_{n+1}^k} - p \frac{\partial p_c}{\partial \epsilon_{n+1}^k} = 0. \quad (4.12)$$

On substitution of (4.8)–(4.10) in (4.12) and by appeal to (2.6),

$$\frac{\partial \Delta \epsilon_v^p}{\partial \epsilon_{n+1}^k} = \beta_1 \mathbf{1} + \beta_2 \hat{n}, \quad (4.13)$$

where

$$\begin{aligned} \beta_1 &= K \left[ \frac{\partial F}{\partial p} \frac{\partial F}{\partial q} \alpha_1 + \left( \frac{\partial F}{\partial p} \right)^2 \right] / \beta, \\ \beta_2 &= 2\mu \left( \frac{\partial F}{\partial p} \frac{\partial F}{\partial q} \alpha_2 \right) / \beta, \\ \beta &= K \left( \frac{\partial F}{\partial p} \right)^2 - K \frac{\partial F}{\partial p} \frac{\partial F}{\partial q} \alpha_3 + \partial p p_c \frac{\partial F}{\partial p}. \end{aligned} \quad (4.14)$$

Substituting (4.13) in (4.8)–(4.10) results in

$$\begin{aligned} \frac{\partial p}{\partial \epsilon_{n+1}^k} &= K(1 - \beta_1) \mathbf{1} - K\beta_2 \hat{n}, \\ \frac{\partial q}{\partial \epsilon_{n+1}^k} &= (\alpha_1 + \alpha_3 \beta_1) \mathbf{1} + (\alpha_2 + \alpha_3 \beta_2) \hat{n}, \\ \frac{\partial p_c}{\partial \epsilon_{n+1}^k} &= p_c \partial \beta_1 \mathbf{1} + p_c \partial \beta_2 \hat{n}. \end{aligned} \quad (4.15)$$

Finally, substituting (4.15) in (4.7) produces the desired consistent tangential tensor

$$\begin{aligned} c_{n+1}^k &= 2\mu \xi \mathbf{I} + [K(1 - \beta_1) - \frac{1}{3}(2\mu)\xi] \mathbf{1} \otimes \mathbf{1} - K\beta_2 \mathbf{1} \otimes \hat{n} + \sqrt{\frac{2}{3}} K(\alpha_1 + \alpha_3 \beta_1) \hat{n} \otimes \mathbf{1} \\ &\quad + [2\mu(\sqrt{\frac{2}{3}} \alpha_2 - \xi) + \sqrt{\frac{2}{3}} \alpha_3 \beta_2 K] \hat{n} \otimes \hat{n}, \end{aligned} \quad (4.16)$$

where  $\xi = \|\xi_{n+1}^k\| / \|\xi_{n+1}^{tr}\|$ . This tensor of tangential moduli is consistent with the linearization of  $\sigma_{n+1}^k$  and results in an iterative solution scheme that preserves the global quadratic convergence in Newton's method.

**REMARK 4.1.** In general,  $\beta \neq -\sqrt{\frac{2}{3}}(\alpha_1 + \alpha_3 \beta_1)$ . Hence, (4.16) results in a nonsymmetric tangent operator.

**REMARK 4.2.** It is of interest to note that under certain conditions the tangential tensor of (4.16) also degenerates to the continuum elastoplastic tensor of (2.11). For example, consider  $\Delta \epsilon_v^p \rightarrow 0$  (i.e., explicit). Under this condition,  $p \rightarrow p_{n+1}^{tr}$ ,  $q \rightarrow q_{n+1}^{tr}$ ,  $p_c \rightarrow (p_c)_n$  and, consequently,  $\xi \rightarrow 1.0$ . Hence,  $\alpha_1 \rightarrow 0$ ,  $\alpha_2 \rightarrow \sqrt{\frac{3}{2}}$ ,  $\alpha_3 \rightarrow -2q(\partial F / \partial p)^{-1}$ ,  $\beta_1 \rightarrow K(\partial F / \partial p)^2 / \beta$ ,  $\beta_2 \rightarrow 2\mu \sqrt{\frac{3}{2}}(\partial F / \partial p)(\partial F / \partial q) / \beta$  and

$$\beta \rightarrow K \left( \frac{\partial F}{\partial p} \right)^2 + K(2q) \frac{\partial F}{\partial q} + \partial p p_c \frac{\partial F}{\partial p}. \quad (4.17)$$

Now, when  $M^2 \rightarrow 1/\theta$  the plastic potential  $Q$  coincides with the yield surface  $F$ . Thus,  $\beta \rightarrow \chi$  (cf. (2.12)) and the flow rule becomes associative. Substituting all these limits in (4.16) results in  $c_{n+1}^k \rightarrow c^{ep}$ , i.e., the consistent tangent given by (4.16) degenerates to the (symmetric) continuum tangent given by (2.9)–(2.11).

#### 4.4. Radial return algorithm

Finally, we consider a radial stress mapping in the deviatoric plane defined by the following scalar equations (see Fig. 3):

$$p = p_{n+1}^{tr}, \quad q = q_{n+1}^{tr} - \Delta q, \quad \text{and} \quad p_c = (p_c)_n, \quad (4.18)$$

where  $\Delta q$  is a scalar consistency parameter,  $p = p_{n+1}^k$ ,  $q = q_{n+1}^k$  and  $p_c = (p_c)_{n+1}^k$ . It can be shown that the plastic potential consistent with this stress integration scheme is given by

$$Q = q - q_c = 0, \quad (4.19)$$

where  $q_c$  is the size of the Mises cylinder generated by (4.19). Since this stress integration scheme predicts no plasticity in bulk, strain hardening will not take place (cf. (2.3)) and the soil is considered to be perfectly plastic.

Imposing the consistency requirement on the yield function  $F = F(\Delta q) = 0$  results in

$$\Delta q = q_{n+1}^{tr} - M \sqrt{-p_{n+1}^{tr}(p_{n+1}^{tr} - p_c)}, \quad 0 \leq p_{n+1}^{tr} \leq p_c. \quad (4.20)$$

Again, writing the stress integration equation thus:

$$\sigma_{n+1}^k = p \mathbf{1} + \sqrt{\frac{2}{3}} q \hat{n}, \quad (4.21)$$

the consistent tangent to (4.21) is evaluated as

$$\begin{aligned} c_{n+1}^k &= \frac{\partial \sigma_{n+1}^k}{\partial \epsilon_{n+1}^k} = 2\mu \xi \mathbf{1} + (K - 2\mu \xi / 3) \mathbf{1} \otimes \mathbf{1} \\ &\quad + K \sqrt{\frac{2}{3}} (p_c - 2p_{n+1}^{tr}) \frac{M^2}{2q} \hat{n} \otimes \mathbf{1} - 2\mu \xi \hat{n} \otimes \hat{n}, \end{aligned} \quad (4.22)$$

where  $\xi = \|\xi_{n+1}^k\| / \|\xi_{n+1}^{tr}\|$ . Note that with this return mapping scheme, only one (global) Newton iteration loop is required for solution. However, although this return mapping scheme is simple to implement, a non-hardening, perfectly plastic constitutive characterization of soils such as described by (4.19) is not considered realistic. Consequently, this return mapping scheme will not be considered in subsequent discussion.

#### 4.5. General remarks on the return mapping schemes

We consider again the closest point projection algorithm of Section 3 and the return mapping scheme given by (3.5) and (3.9) (see e.g. [7]). It can be shown that, depending on

the values of  $\theta = K/(3\mu)$ , the closest point projection algorithm described in Section 3 (in the metric defined by  $c^e$ ) also leads to various geometric return mapping schemes on the ellipsoids shown in Fig. 4. This point can be illustrated by considering the return direction

$$\frac{p_{n+1}^{tr} - p}{q_{n+1}^{tr} - q} = \frac{\Delta p}{\Delta q} = \frac{K\Delta\epsilon_v^p}{3\mu\Delta\gamma^p} = -\theta \frac{dq}{dp}, \quad (4.23)$$

where

$$\frac{\Delta\epsilon_v^p}{\Delta\gamma^p} = -\frac{dq}{dp} = M^2 \left( \frac{p - \frac{1}{2}p_c}{q} \right) \quad (4.24)$$

by virtue of the associative flow rule. Substituting (4.24) in (4.23) yields

$$\frac{\Delta p}{\Delta q} = \theta M^2 \left( \frac{p - \frac{1}{2}p_c}{q} \right), \quad q \neq 0, \quad (4.25)$$

which implies the dependence of the return direction on the elastic moduli ratio  $\theta$ . As an illustration, the condition  $\theta \rightarrow \infty$  implies elastic incompressibility so that  $\Delta q \rightarrow 0$  and results in the associative flow rule leading to a hydrostatic return to the ellipsoid  $F$ ; the condition  $\theta = M^{-2}$  results in (4.23) and (4.25) degenerating to (4.1b) and leads to a central return; the condition  $\theta = 1.0$  is equivalent to a geometric closest point projection on the ellipsoid  $F$ ; finally, the condition  $\theta = 0$  leads to  $\Delta p = 0$ , or a radial return. These return mapping directions are summarized in Fig. 4.

Note from (4.23) that as the critical state limit is reached,  $\Delta\epsilon_v^p \rightarrow 0$  and the soil becomes plastically incompressible. In general, plastic incompressibility does not require a special algorithmic treatment provided that  $\kappa > 0$  and the soil is loaded 'drained'. In this case, the soil becomes perfectly plastic (non-hardening) but remains elastically compressible.

Finally, it is worth noting that since the pressure-dependent elastic moduli are computed explicitly, then 'Hooke's law'

$$\sigma_{n+1} = c_{n+1}^e : (\epsilon_{n+1} - \epsilon_{n+1}^p) \quad (4.26)$$

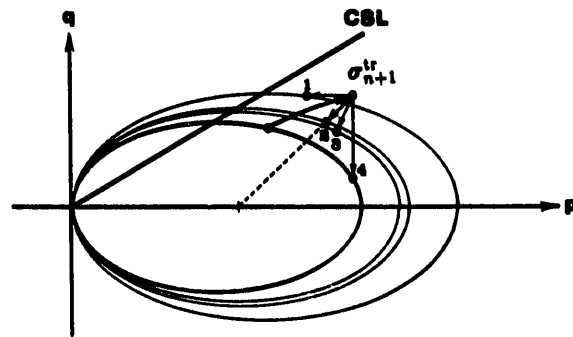


Fig. 4. Various return mapping directions for associative flow rule: 1. hydrostatic return, 2. central return, 3. closest point projection on  $F$ , 4. radial return.



is violated at  $t_{n+1}$ , with  $\epsilon_{n+1}^p$  computed implicitly. In fact, because  $c^e$  is stress-dependent, the 'true' solution at time  $t_{n+1}$  does not really satisfy (4.26). This fact follows directly from the rate constitutive equation

$$\dot{\sigma} = c^e : (\dot{\epsilon} - \dot{\epsilon}^p). \quad (4.27)$$

Taking the volumetric parts of (4.27) yields

$$\dot{p} = K(\dot{\epsilon}_v - \dot{\epsilon}_v^p) = K\dot{\epsilon}_v^e. \quad (4.28)$$

Using the instantaneous value of  $K$  from (2.13) and integrating (4.28) over  $[t_n, t_{n+1}]$  yields (again, setting  $e = e_n$  over this time step)

$$p_{n+1} = p_n \exp \left( \frac{1 + e_n}{\kappa} \Delta \epsilon_v^e \right), \quad (4.29)$$

which shows an exponential variation of  $p_{n+1}$  with respect to the incremental strain  $\Delta \epsilon_v^e$ , as opposed to the linear equation (4.26).

## 5. Numerical examples

Two subprograms named CLSEST and CNTRAL were written to investigate the performance of the closest point projection and the central return mapping algorithms with respect to accuracy and stability. Since these algorithms are intended for global applications, we focus on the performance of these algorithms in the large, rather than simply concentrate on one specific Gauss point. The two subprograms were linked to a nonlinear finite element main program called DIG-DIRT [18] which solves a system of nonlinear equations by Newton-Raphson iterations. Iterations are terminated according to the following convergence criteria:

### 1. Residual force criterion:

$$\|r^k\| \leq \epsilon_R \|r^0\|. \quad (5.1)$$

### 2. Energy criterion:

$$|\Delta d^k \cdot r^k| \leq \epsilon_E |\Delta d^0 \cdot r^0|, \quad (5.2)$$

where  $r^k = (F_{\text{EXT}})_{n+1} - F_{\text{INT}}(\sigma_{n+1}^k)$ ,  $F_{\text{EXT}}$  is the external force vector,  $F_{\text{INT}}$  is the internal force vector and  $\Delta d^k$  is the search direction, and where the symbol  $\|\cdot\|$  denotes an  $L_2$ -vector norm and  $|\cdot|$  denotes absolute values taken. The force and energy thresholds were set at  $\epsilon_R = 10^{-3}$ ,  $\epsilon_E = 10^{-5}$ , while the local and sub-local convergence tolerances contained in Tables 1–3 were set at  $\text{FTOL} = \text{GTOL} = 10^{-5}$ . All computations were performed using 72-bits per double precision floating point word at Stanford University's LOTS System.

Initial stresses were generated internally according to the following procedure. First, small isotropic compressive stresses were generated at each integration point (in the order of about 1 percent of the final gravity-induced stresses) and gravity loads were applied in three steps as depicted in the stress path shown in Fig. 5 (it must be noted that since the elastic moduli  $K$  and  $\mu$  are directly proportional to the volumetric stress  $p$ , and since these moduli are treated explicitly, non-zero initial compressive stresses are required as input to get the solution started). Next, the elements were preloaded with a uniform surcharge applied in one step, which is subsequently removed, thereby establishing a soil profile that is heavily overconsolidated on top and nearly normally consolidated at greater depths (in the present context, the degree of overconsolidation of a Gauss point in a soil mass is defined as  $OCR = p_c/p_0$ , where  $p_c$  is the current size of the ellipsoid at the Gauss point in question and  $p_0 = p + q^2/(M^2 p)$  is the 'equivalent preconsolidation pressure' corresponding to the current state of stress ( $p, q$ ) at this same point [2]). This has the effect of realistically simulating initial stress states of soils in a 'geostatic' state [19]. The soil considered is Undisturbed Bay Mud having a unit weight of  $\gamma = 20 \text{ kN/m}^3$  and the following Cam-Clay parameters [9]:  $M = 1.4$ ,  $\lambda = 0.37$ ,  $\kappa = 0.054$ ,  $e_a$  = reference void ratio at unit preconsolidation = 2.52, and elastic Poisson's ratio  $\nu \approx 0.35$ , which gives the relationship  $K \approx 3\mu$ .

**EXAMPLE 1. Bearing capacity of Bay Mud.** In this example, we consider a strip footing of width  $B$  subjected to a line load of intensity  $P$  applied at an eccentricity of  $e = 0.1 B$  and inclined at  $20^\circ$  relative to the vertical axis. The footing is assumed to be infinitely stiff (rigid punch). The mesh, shown in Fig. 6, is composed of 200, four-noded quadrilateral 'soil' elements and 6 'footing' elements with a  $2 \times 2$  Gaussian integration rule employed for each element. The load  $P$  is applied in one, two, five and twenty equal steps up to a maximum value of  $80 \text{ kN/m}$  representing about 95 percent of the full value of the failure load. Stresses were integrated using subprograms CLSEST and CNTRAL and the solutions obtained from these two schemes were compared.

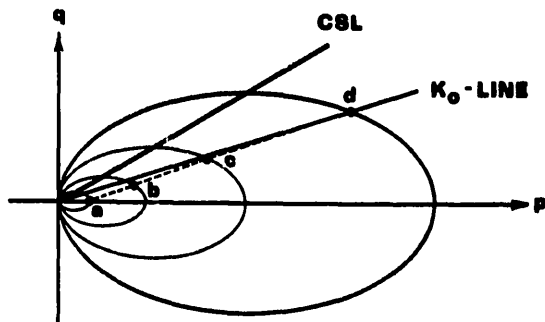


Fig. 5. Gravity load imposition for the Cam-Clay problem: isotropic starting point at  $a$ , then loaded in three steps along the  $K_0$ -line  $b, c, d$  (constrained compression).

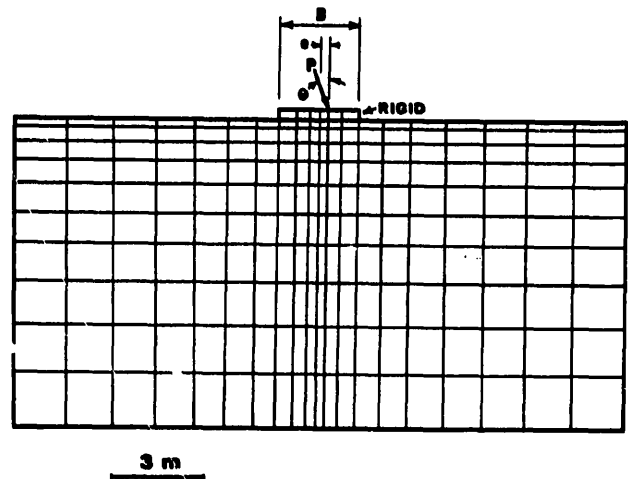


Fig. 6. Bearing capacity of Bay Mud: finite element mesh.

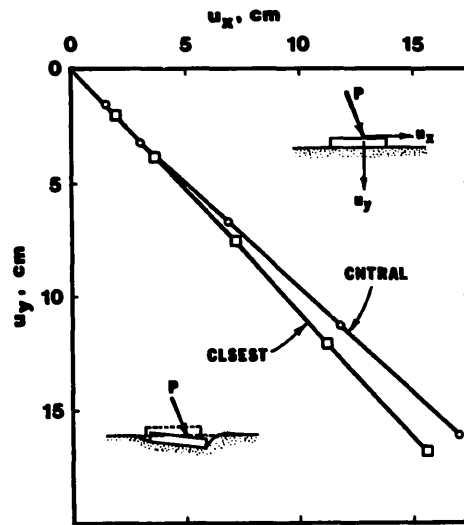


Fig. 7. Displacement history for the rigid punch problem: solid lines denote 20-step solutions, discrete points denote 5-step solutions.

Figure 7 shows the displacement histories of the application point of the line load  $P$  predicted by the subprograms CLSEST and CNTRAL. Both return mapping schemes predicted considerable plastic volumetric deformation developing beneath the footing characterized by punching with very little heaving of the ground surface (Fig. 7), as opposed to typical ground displacements obtained from solutions based on incompressible plasticity models (see e.g. [20, 21]).

Tables 4 and 5 demonstrate the accuracy of the two stress integration algorithms and show

Table 4

Rigid punch problem: final displacement of point A for Cam-Clay plasticity with associative flow rule

Number of time steps	Ave. no. iterations per time step	$u_x$ , meters	$u_y$ , meters	CPU sec.
1	# <sup>a</sup>	# <sup>a</sup>	# <sup>a</sup>	# <sup>a</sup>
2	14.5	0.17	-0.18	477
5	5.8	0.15	-0.17	496
20	4.0	0.15	-0.17	920

<sup>a</sup>did not converge after 20 iterations.

Table 5

Rigid punch problem: final displacement of point A for Cam-Clay plasticity with a non-associative flow rule

Number of time steps	Ave. no. iterations per time step	$u_x$ , meters	$u_y$ , meters	CPU sec.
1	# <sup>a</sup>	# <sup>a</sup>	# <sup>a</sup>	# <sup>a</sup>
2	15.5	0.18	-0.17	457
5	6.6	0.17	-0.16	489
20	3.9	0.16	-0.16	899

<sup>a</sup>did not converge after 20 iterations.

that the five and twenty step solutions gave nearly identical results for each scheme. Note from these tables that the two-step solution for displacements differs from the twenty step solution only by about 10 percent, although more iterations per load step were required by the two-step solution. The one-step solution diverged, not surprisingly, considering that the elastic moduli were computed explicitly in the formulation and that the total load applied was close to the failure load.

Tables 4 and 5 also show the average number of iterations required for convergence for each of the two integration algorithms and the total CPU required for execution. Both algorithms required practically the same number of iterations for convergence for a given step size. The closest point projection algorithm, which had three nested Newton iteration loops, required only about 3 to 5 percent more CPU than the central return mapping algorithm which had two nested Newton iteration loops. Numerical experiments revealed that only three to four scalar iterations were required for the innermost loop in the subprogram CLSEST to converge according to a (stringent) error tolerance of  $GTOL = 10^{-5}$  in Table 2. Thus, it is seen from this example that the three-nested-loop feature of the proposed closest point projection algorithm is not its drawback.

Figure 8 shows the generation of zones of plastification predicted by the subprogram CLSEST corresponding to 40, 60, 80 and 100 percent of the full value of the applied line load obtained from the five-step solution. For reference, the initial overconsolidation profile is likewise shown in this figure. Except for points in the vicinity of the footing, the soil crust is seen to have remained overconsolidated during this loading process. For completeness, Table 6 demonstrates the rate of convergence in energy norms from the five-step solution exhibited by the two stress integration schemes.

**EXAMPLE 2. Plane strain excavation in Bay Mud.** As a second example, we consider the mesh shown in Fig. 9 composed of 80, four-noded quadrilateral elements with the same  $2 \times 2$  standard Gaussian rule employed for integrating stresses. The soil considered is the same Bay Mud used in Example 1. Initial conditions consisting of gravity imposition and preloading were established following the same procedures described earlier. For reference, the initial OCR profile is shown in Fig. 10.

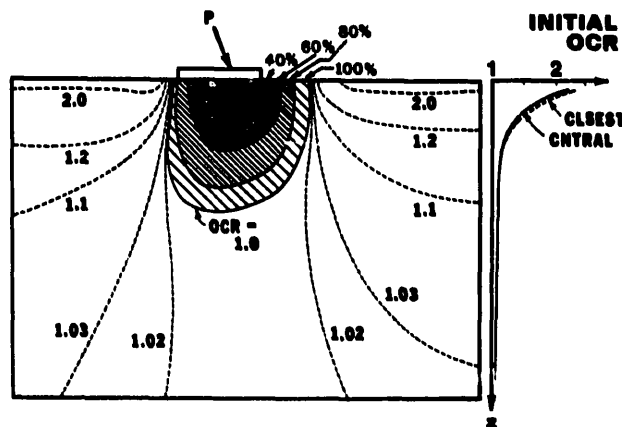


Fig. 8. Rigid punch problem: zones of plastification and contour of initial and final OCR.

Table 6

Rigid punch, eccentric and inclined load: energy norm values for step 2 of the 5-step solution

Iteration number	CLSEST	CNTRAL
1	1.000e + 0	1.000e + 0
2	4.150e - 1	5.002e - 1
3	5.751e - 2	1.016e - 1
4	5.935e - 4	3.065e - 3
5	1.757e - 7	4.340e - 7

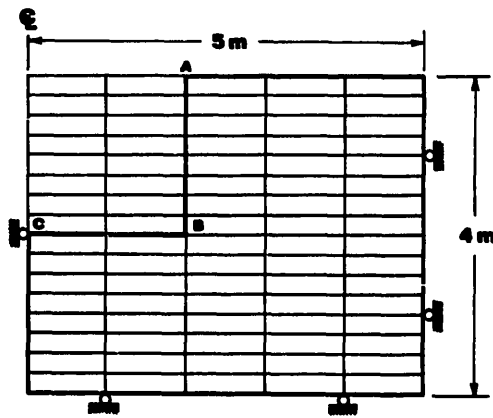


Fig. 9. Finite element mesh for the plane strain and axisymmetric excavation problems.

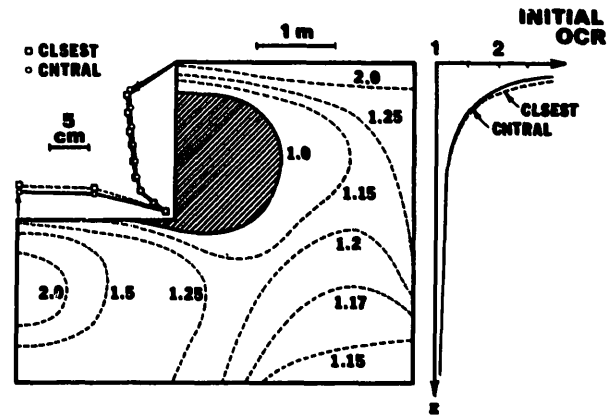


Fig. 10. Plane strain excavation: final excavation-induced displacements and zone of plastification; initial and final OCR contour also shown.

In estimating the excavation-induced displacements in a vertical cut, one is usually concerned about the sensitivity of the solution to the number of 'lifts' employed to get to the final stage. By definition, the true final stage solution is one which entails the removal of infinitesimally thin layers of elements sequentially until the final height of the vertical cut is reached. The accuracy of a stress integration algorithm can then be assessed by looking at the 'error' generated as a result of removing these layers in finite increments.

In this example, the sixteen elements shown in Fig. 9 were removed (i.e., excavated) in one, two, four and eight lifts corresponding to the removal of sixteen, eight, four and two elements at a time using the element-death analysis algorithm proposed in [18]. The eight-step solution is then the 'correct' solution for this (coarse) mesh to which solutions with fewer number of steps will tend.

Tables 7 and 8 show the final excavation-induced displacements at point A in an upper corner of the post-excavation domain shown in Fig. 10, assuming a condition of plane strain. Between the four- and the eight-step solutions the discrepancies are minimal (about 4% for  $u_x$  and 3% for  $u_y$ ), although the 'error' for the one-step solution is not insignificant. Again, Tables 8 and 9 show that both integration algorithms required practically the same number of

Table 7

Plane strain excavation problem: final displacement of point A for Cam-Clay plasticity with associative flow rule

Number of lifts	Ave. no. iterations per lift	$u_x$ , meters	$u_y$ , meters	CPU sec.
1	5.0	-0.042	-0.015	93
2	3.5	-0.047	-0.020	97
4	2.5	-0.050	-0.023	104
8	2.5	-0.052	-0.024	126

Table 8

Plane strain excavation problem: final displacement of point A for Cam-Clay plasticity with a non-associative flow rule

Number of lifts	Ave. no. iterations per lift	$u_x$ , meters	$u_y$ , meters	CPU sec.
1	5.0	-0.059	-0.023	78
2	3.0	-0.065	-0.029	82
4	2.8	-0.069	-0.032	93
8	2.8	-0.072	-0.033	117

iterations to converge, with the subprogram CLSEST needing only about 15 percent more CPU than the subprogram CNTRAL.

Figure 10 shows the displacement profile at the base and along the vertical face of the resulting long, rectangular pit generated, assuming a condition of plane strain. This figure also shows heaving of the soil at the base resulting in the development of a local overconsolidated zone beneath the base. Considerable plastification is noted in the vicinity of the bottom corner denoted by the shaded region characterized by an overconsolidation ratio of  $OCR = 1.0$ . However, the soil crust remained overconsolidated during this excavation process. Residual force norms are tabulated in Table 9 for the one-step excavation to demonstrate the rate of convergence of the iterative solutions.

Table 9

Plane strain vertical cut problem: residual force norm values for the one-step excavation

Iteration number	CLSEST	CNTRAL
0	1.000e + 0	1.000e + 0
1	1.261e - 1	1.431e - 1
2	5.702e - 2	6.154e - 2
3	4.688e - 3	2.706e - 2
4	7.439e - 4	1.419e - 3
5	7.580e - 5	4.425e - 6
6	4.572e - 10	4.167e - 11

**General Remarks on Stability.** Cam-Clay models are particularly vulnerable to numerical breakdown [4] and, therefore, great care is usually required in choosing a step size that will lead to a convergent solution. In general, the two integration algorithms described in this paper could lead to a divergent solution when (a) the step size is unreasonably large, such as the one-step solution in Example 1, and (b) the input initial stresses necessary in defining the initial elastic moduli during the gravity load imposition phase are not proportional to depth (e.g., uniform). We observed that input initial stresses should be approximately proportional to depth so that the Gauss points near the ground surface and those at greater depths will be subjected to proportional incremental (gravity) loads, thus enhancing convergence.

From the above numerical examples, it is seen that gravity loads are an essential part of a Cam-Clay solution because the elastic moduli  $c^e$  and the hardening parameter  $p_c$  both depend on these initial stresses, unlike in simpler plasticity models such as the Von Mises and Drucker-Prager models where gravity loads do not play a major role. Much of the difficulty will more likely arise during this gravity load imposition phase and, therefore, great care should be exercised in choosing an appropriate step size (we observed that subdividing the gravity loads into three increments of 10, 20 and 70 percent, in that order, will often lead to a convergent solution). Once the initial, gravity-induced stresses had been established, however, the two algorithms generally showed marked stability as exemplified by the two-step solution of Example 1 and the one-step excavation of Example 2.

## 6. Concluding remarks

Two stress integration algorithms based on implicit calculation of plastic strains were implemented and tested for the modified Cam-Clay plasticity model. Numerical examples were presented to demonstrate the global accuracy and stability of these techniques and their applications to geotechnical engineering problems such as foundation bearing capacity and sequential excavation. Both schemes entail an iterative determination of the consistency parameter and the tangent operator on the scalar level, and are amenable to exact linearization. The relationships among various return mapping schemes were established in the context of associative and non-associative flow rule formulations.

## Acknowledgement

Financial support was provided in part by the U.S. National Foundation under Contract No. MSS-8910219, Research Initiation Award. Computer time was provided by Stanford University's LOTS System.

## References

- [1] J.H. Atkinson, *Foundations and Slopes: An Introduction to Applications of Critical State Soil Mechanics* (Halsted Press, New York, 1981).

- [2] R.I. Borja and E. Kavazanjian, Jr., A constitutive model for the stress-strain-time behaviour of 'wet' clays, *Géotechnique* 35 (3) (1985) 283-298.
- [3] R.I. Borja and E. Kavazanjian, Jr., Finite element analysis of the time-dependent behavior of soft clays, *Geotech. Engrg. Res. Report No. GT1*, Stanford University, 1984.
- [4] A. Gens and D.M. Potts, Critical state models in computational geomechanics, *Engrg. Comp.* 5 (1988) 178-197.
- [5] M. Ortiz and J.C. Simo, An analysis of a new class of integration algorithms for elastoplastic constitutive relations, *Internat. J. Numer. Methods Engrg.* 23 (1986) 353-366.
- [6] K.H. Roscoe and J.B. Burland, On the generalized stress-strain behavior of 'wet' clay, in: J. Heyman and F.A. Leckie, eds., *Engineering Plasticity* (Cambridge Univ. Press, Cambridge, 1968) 535-609.
- [7] K. Runesson, Implicit integration of elastoplastic relations with reference to soils, Short communication, *Internat. J. Numer. Analyt. Methods Geomech.* 11 (1987) 315-321.
- [8] A. Schofield and P. Wroth, *Critical State Soil Mechanics* (McGraw-Hill, New York, 1968).
- [9] R. Bonaparte and J.K. Mitchell, The properties of San Francisco Bay Mud at Hamilton air force base, California, *Geotech. Engrg. Res. Report*, University of California, Berkeley, 1979.
- [10] D.R. Owen and E. Hinton, *Finite Elements in Plasticity: Theory and Practice* (McGraw-Hill, New York, 1980).
- [11] T.J.R. Hughes, Numerical implementation of constitutive models: rate independent deviatoric plasticity, Workshop on Theoretical Foundations for Large Scale Computations on Nonlinear Material Behavior, Northwestern University, Evanston, Illinois, 1983.
- [12] R.D. Krieg and S.W. Key, Implementation of a time dependent plasticity theory into structural computer programs, in: J.A. Stricklin and K.J. Saczalski, eds., *Constitutive Equations in Viscoplasticity: Computational and Engineering Aspects*, AMD-20 (ASME, New York, 1976).
- [13] J.C. Simo and R.L. Taylor, Consistent tangent operators for rate-independent elastoplasticity, *Comput. Methods Appl. Mech. Engrg.* 48 (1985) 101-118.
- [14] J.C. Simo, J.W. Ju and R.L. Taylor, Softening response, completeness condition and numerical algorithms for the cap model, *Internat. J. Numer. Methods Engrg.*, to appear.
- [15] M.L. Wilkins, *Calculation of Elastic-plastic Flow*, *Methods of Computational Physics* 3 (Academic Press, New York, 1964).
- [16] Z. Mroz, V.A. Norris and O.C. Zienkiewicz, Application of an anisotropic hardening model in the analysis of elasto-plastic deformation of soils, *Géotechnique* 29 (1) (1979) 1-34.
- [17] M. Zytinsky, M.K. Randolph, R. Nova and C.P. Wroth, On modeling the unloading-reloading behaviour of soils, *Internat. J. Numer. Analyt. Methods Geomech.* 2 (1978) 87-93.
- [18] R.I. Borja, S.R. Lee and R.B. Seed, Numerical simulation of excavation in elastoplastic soils, *Internat. J. Numer. Analyt. Methods Geomech.* 13 (1989) 231-249.
- [19] T.W. Lambe and R.V. Whitman, *Soil Mechanics* (Wiley, New York, 1969).
- [20] R. Hill, *The mathematical theory of plasticity* (Oxford Univ. Press, Oxford, 1950).
- [21] J.H. Prevost, Localization of deformations in elastic-plastic solids, Short communication, *Internat. J. Numer. Analyt. Methods Geomech.* 8 (1984) 187-196.